Energy 338 (2025) 138815

Contents lists available at ScienceDirect

Energy

journal homepage: www.elsevier.com/locate/energy

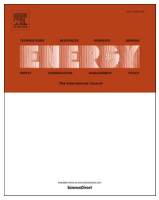

Semi-physical experimental research for active control of high-frequency combustion oscillation based on dual spool fuel valve

Chengyuan Li, Yuchuan Zhu *

College of Mechanical and Electrical Engineering, Nanjing University of Aeronautics and Astronautics, Nanjing, 210016, Jiangsu, China

ARTICLE INFO

Keywords:
High-frequency combustion oscillation
Active control
Dual spool fuel valve
Semi-physical experiment
H-infinity control algorithm
Disturbance observer

ABSTRACT

Lean pre-mixed pre-vaporized combustion technology possesses the capability to markedly improve combustion efficiency and reduce pollutant emissions in aeroengines. Nevertheless, it may also lead to combustion oscillation, which pose a considerable risk to flight safety. The utilization of active control through a high-frequency fuel valve has been recognized as the most efficient method for suppressing combustion oscillation. However, it necessitates that the fuel valve possesses the ability to perform high-frequency and large-amplitude flow regulation, maintaining a compact design, and is capable of enduring high-temperature environments. To verify that a dual spool fuel valve (DSFV) satisfies the requirements of the active control system and effectively suppresses multimodal combustion oscillations, this paper presents a semi-physical experimental system that utilizes a DSFV prototype and a high-frequency combustion oscillation model. Furthermore, the paper proposes the H-infinity combined disturbance observer control strategy to improve the robustness of the system. The experimental results indicated that the system achieved an average suppression effect of 61 % in the amplitudes of multimodal oscillating pressures under non-oil flowing conditions and an average suppression effect of 62.5 % under oil flowing conditions.

1. Introduction

The development of efficient and environmentally sustainable aviation propulsion technologies has led to the widespread implementation of lean pre-mixed pre-vaporized combustion technology aimed at improving combustion efficiency and reducing pollutant emissions [1,2]. Nonetheless, this methodology is prone to the coupling of unsteady heat release and acoustic fluctuations within the combustion chamber, which can ultimately lead to combustion oscillation [3,4]. Such oscillation may adversely affect combustion efficiency, exacerbate engine vibrations, jeopardize the structural integrity of the engine, and potentially lead to engine shutdowns, thereby presenting considerable risks to both engine safety and reliability [5,6].

In accordance with the Rayleigh criterion, strategies for suppressing combustion oscillation can be classified into two primary categories: passive and active control methods [7,8]. Passive control methods focus on augmenting acoustic damping within the combustion chamber to enhance acoustic dissipation. These methods typically involve the use of Helmholtz resonators [9,10], acoustic liners [11,12], and baffle blade [13]. Conversely, active control methods aim to disrupt the coupling between unsteady heat release and acoustic fluctuations through introducing external energy into the combustion chamber, thereby diminishing the acoustic energy produced by unsteady combustion. Common active control methods include the acoustic modulation utilizing loudspeakers [14,15] and the regulation of fuel flow via fuel valves [16–18]. Usually, the passive control methods require alterations to the combustion chamber's structures and show limited flexibility in addressing various combustion oscillation modes. Furthermore, the loudspeaker-based active control method is limited by the challenges posed by high-temperature and high-pressure conditions present in the combustion chamber. Conversely, the fuel valve-based active control method does not require any structural alterations to the combustion chamber and exhibits significant adaptability to various combustion oscillation modes, making it the most practical and effective method to suppress combustion oscillation.

A typical fuel valve-based active control system is fundamentally composed of three key elements: sensor, controller, and fuel valve. While there have been notable advancements in high-temperature and

* Corresponding author. College of Mechanical and Electrical Engineering, Nanjing University of Aeronautics and Astronautics, No. 29, Yudao street, Qinhuai District, Nanjing, 210016, China.
E-mail address: meeyczhu@nuaa.edu.cn (Y. Zhu).

https://doi.org/10.1016/j.energy.2025.138815
Received 28 May 2025; Received in revised form 30 September 2025; Accepted 7 October 2025
Available online 8 October 2025

high-precision sensing technologies [19,20] and sophisticated active control algorithms [21–25], the development of the fuel valve has progressed at a comparatively slower pace. The primary reason is that the dominant frequency of combustion oscillation in aeroengines is approximately 600 Hz, which necessitates that the fuel valve be capable of high-frequency and large-amplitude flow regulation. Additionally, due to the constraints imposed by limited installation space and the high-temperature environment of aeroengine, the fuel valve must be compact in design and capable of operating effectively under high-temperature conditions. Current fuel valves, whether driven by electromagnetic or smart materials, fail to concurrently satisfy all necessary specifications. Ref. [26]presented an electromagnetic actuator capable of a stroke of up to 450 μm; however, it is constrained by a bandwidth of merely 300 Hz. Similarly, ref. [27] enhanced the design of an electromagnetic actuator, achieving a bandwidth of only 350 Hz. Ref. [28] introduced a magnetostrictive fuel valve with a bandwidth of 1000 Hz and an operational temperature of 148 °C. Nonetheless, the inherent strain characteristics of magnetostrictive materials, which typically do not exceed 0.2 %, result in a valve length that surpasses 45.7 cm. Furthermore, ref. [29] developed a piezoelectric fuel valve measuring 7.1 cm in length and possessing a bandwidth of 1000 Hz. However, the piezoelectric actuator cannot function effectively under high-temperature conditions.

In response to the need for fuel valve in the active control system of high-frequency combustion oscillation, our prior research led to the development of a dual spool fuel valve (DSFV) [30]. This innovative valve is capable of concurrently regulating the average flow for routine flight operations and the high-frequency flow necessary for active control. With a compact length of only 13.9 cm, simulation results demonstrate its ability to generate a high-frequency flow of 4.7 L/min at a frequency of 1000 Hz. The high-frequency flow is regulated by the inner spool, which is actuated by a multidimensional discrete magnetostrictive actuator (MDMA) [31]. Experimental results indicate that the MDMA achieves an output displacement of 101 μm with a volume of 163 cm^3 and a mass of 787 g, a frequency bandwidth exceeding 1000 Hz, and a displacement attenuation of less than 13 % at an ambient of 120 °C [32]. The DSFV satisfies the requirements for high-frequency and large-amplitude flow regulation, compact size, and high operating temperatures. Nevertheless, it remains imperative to perform active control experiments in order to validate its efficacy to suppress combustion oscillation.

Generally, research on the active control of combustion oscillation is conducted utilizing real engines [33,34], combustion rigs [35,36], Rijke tubes [37,38], and simulation models [39]. While full physical experiments provide reliable and authentic results, they are often associated with high costs and limited flexibility. Conversely, full model simulations present economic advantages, but the confidence in their results tends to be comparatively low. Semi-physical experiments effectively combine the advantages of both full physical experiments and full model simulations, thereby offering enhanced efficiency and safety, as well as facilitating rapid validation of principle. Consequently, the semi-physical experimental system, developed in accordance with the DSFV prototype and combustion oscillation model, can be employed to a certain degree to validate the efficacy of the DSFV to suppress combustion oscillation.

In the semi-physical experimental system, the combustion oscillation model plays a crucial role in determining the confidence level of the experimental results. This model is typically established through two principal methodologies. The first methodology relies on the thermal-acoustic coupling relationship, which decouples the acoustic fluctuations and the unsteady heat release [23,40]. It calculates the amplitudes of acoustic fluctuations via wave equations and calculates the unsteady heat release through either a linear flame transfer function or a nonlinear flame description function. The second methodology establishes the transfer functions for both the acoustic model and the flame model, which are subsequently integrated with the saturation non-linearity to form the combustion oscillation model [35,41]. Both methodologies describe the phenomenon of pressure oscillations induced by thermal-acoustic coupling within the combustion chamber, ultimately reaching saturation. However, the model established by the first methodology necessitates considerable computational resources, rendering it insufficient for the real-time computational requirements of the semi-physical experiments. In contrast, the combustion oscillation model that utilizes transfer functions exhibits superior real-time performance and was established using empirical high-frequency oscillation measurement data of actual aeroengine, thereby augmenting its reliability. Additionally, by modifying the parameters of the model, it is possible to alter the oscillation modes, which in turn supports further investigation into the suppression effects of multimodal oscillating pressures.

Active control algorithms are essential for suppressing combustion oscillation. Initially, active control strategies predominantly utilized phase-shift [42,43] and PID controllers [44], but these approaches demonstrate limited robustness and adaptability across various combustion oscillation modes. In response, contemporary active control algorithms have emerged, drawing upon optimal control theory and intelligent control principles. Notable examples include Linear Quadratic Regulator control algorithms [21], Model Predictive Control algorithms [22], and neural network-based control algorithms [23]. Despite their advancements, the efficacy of these algorithms is contingent upon the availability of accurate combustion oscillation models, which presents considerable challenges for practical engineering applications. H-infinity control represents a linear control strategy that proficiently mitigates specific modeling inaccuracies and external disturbances, and it has been utilized in the active control of combustion oscillation [24,25]. In this study, the errors between the physical and nominal model of the DSFV system, the disturbances caused by friction and hydraulic forces on the displacement of the inner spool, and the discrepancies of multimodal combustion oscillations impose stringent requirements on the robustness of the control system. The DOB interprets the discrepancy between the anticipated and actual outputs as equivalent disturbances and implements compensation at the input to alleviate these disturbances. Ref. [45] developed a DOB aimed at enhancing the disturbance rejection capability and control precision of the flexible spacecraft attitude maneuvering control system, effectively addressing external disturbances and vibrations induced by flexible attachments during maneuvers. Ref. [46] regarded the hysteresis nonlinearity of piezoelectric actuators as a disturbance to the linear system and utilized a DOB to estimate and compensate for this hysteresis nonlinearity.

Therefore, the innovative contribution of this paper is the development of a semi-physical experimental system for active control of high-frequency combustion oscillation, based on the DSFV prototype and the combustion oscillation model, and proposal of the H-infinity combined DOB control strategy to improve the robustness of the system. The results indicate that the active control system is capable of effectively suppressing multimodal combustion oscillations under different operating conditions.

The remainder of this paper is structured as follows: The architectures and working principles of the MDMA and DSFV are shown in Section 2. In Section 3, the compositions and working principle of the semi-physical experimental system are explained in detail, along with the design of each model within the system. Furthermore, the DSFV prototype and the semi-physical experimental platform are introduced in this section. Section 4 provides a detailed analysis of the experimental results. Section 5 gives the conclusion.

2. Architectures and working principles of the MDMA and DSFV

2.1. Architecture and working principle of the MDMA

As depicted in Fig. 1, the MDMA is composed of three primary

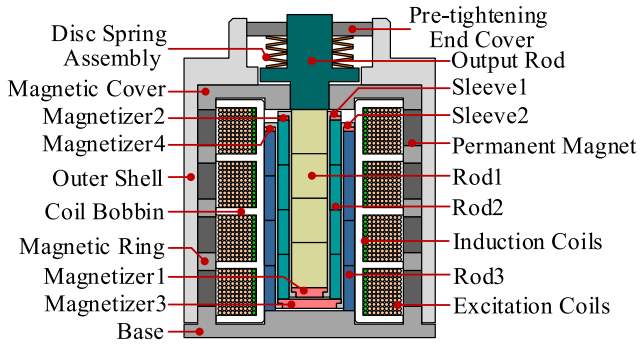

Fig. 1. The architecture of the MDMA.

components: the Multidimensional Discrete Magnetostrictive Stack (MDMS), the Discrete Electromagnetic Excitation Mechanism (DEEM), and the Preload Application Mechanism (PAM). The MDMS is constructed from three magnetostrictive rods, two sleeves, and four magnetizers. The DEEM features four sets of excitation coils and four permanent magnets, which generate a bias magnetic field to eliminate the frequency-doubling effect commonly associated with magnetostrictive materials. Furthermore, the induction coils integrated within the excitation coils are designed to obtain the displacement of MDMA through self-sensing. The PAM, which consists of a disc spring assembly, an output rod, and a pre-tightening end cover, is employed to adjust the preload, thereby optimizing the output performance of the MDMA.

The working principle of the MDMA is illustrated in Fig. 2, which outlines the conversion process of various physical quantities. The voltage generated by the signal generator is converted into current within the excitation coils through four power amplifiers. The axially discrete configuration effectively diminishes the inductive reactance of the excitation coils, thereby improving the response speed of the voltage-to-current conversion process. The excitation magnetic field is superimposed on the bias magnetic field, resulting in a magnetic field distribution that is confined by the closed magnetic circuit formed by the magnetic conductive components and the MDMS. This magnetic interaction induces magnetization in the magnetostrictive rods, generating magnetostrictive strain and ultimately producing magnetostrictive force. The multibody dynamic systems of the MDMS and PAM work in concert to facilitate displacement output driven by this magnetostrictive force. Importantly, the axially discrete structure enhances the dynamic characteristics during the magnetization of the rods, while the radially discrete configuration facilitates large-amplitude displacement of the magnetostrictive rods. This multidimensional discrete architecture ultimately enables the MDMA to achieve high-frequency and large-amplitude displacement within spatial constraints.

2.2. Architecture and working principle of the DSFV

The architecture of the DSFV is depicted in Fig. 3. This valve employs a two-position, two-way sliding valve configuration characterized by radially nested spools. Both the inner and outer spools are capable of axial movement, which collectively regulates the orifice opening.

The outer spool, which is driven by a voice coil motor (VCM), generates an average flow that adequately satisfies the routine fuel supply requirements of the aeroengine through low-frequency and large-amplitude motion. Conversely, the inner spool, driven by an MDMA, generates a high-frequency oscillating fuel flow that facilitates the active control of combustion oscillation through high-frequency and small-amplitude motion. The total fuel flow of the DSFV is the result of the superposition of both the average and oscillating flows.

3. Semi-physical experimental system

3.1. System compositions and working principle

As illustrated in Fig. 4, the semi-physical experimental system comprises four power amplifiers, a DSFV prototype, analog signal input/output modules, a filter model, a displacement-flow transfer model, a flow-pressure transfer model, a combustion oscillation model, a DOB model, and an active controller model. The physical components include the power amplifiers and the DSFV prototype, collectively referred to as the DSFV system. All models were integrated into a real-time simulator, which was connected to a monitor for the purpose of recording the experimental results.

Due to the inability to accurately measure the high-frequency oscillating flow at 1000 Hz, this paper derived the theoretical high-frequency oscillating flow of the DSFV through measuring the displacement of the inner spool and integrating it with the displacement-flow transfer model.

In the semi-physical experimental system, the combustion oscillation model is utilized to generate a high-frequency oscillating pressure p_1, which reaches saturation within the combustion chamber. Upon activation of the switch, the active controller receives the oscillating pressure signal p_3 and subsequently produces a control signal u. This control signal u is then transmitted to the power amplifiers via the analog signal output module, where it is converted into a current i within the excitation coils, thereby facilitating the movement of the inner spool. The displacement signal y of the inner spool is transmitted to the filter model through the analog signal input module, where it undergoes filtering to reduce sampling noise. The DOB is employed to monitor and compensate for the discrepancies between the actual and the anticipated output of the inner spool. The displacement-flow transfer model is responsible for calculating the high-frequency oscillating mass flow Q_m generated by the motion of the inner spool. Following this, the flow-pressure transfer model computes the high-frequency oscillating pressure p_2, which results from the high-frequency oscillating mass flow Q_m after undergoing tube transportation, fuel-air mixing, spray atomization, and combustion processes. If the pressures p_1 and p_2 are in opposing phases, the oscillating pressure p_3 exhibits a continuous decrease, effectively suppressing the combustion oscillation. Additionally, the inlet pressure p_{in}, outlet pressure p_{out}, flow rate Q, and excitation coil current i are recorded

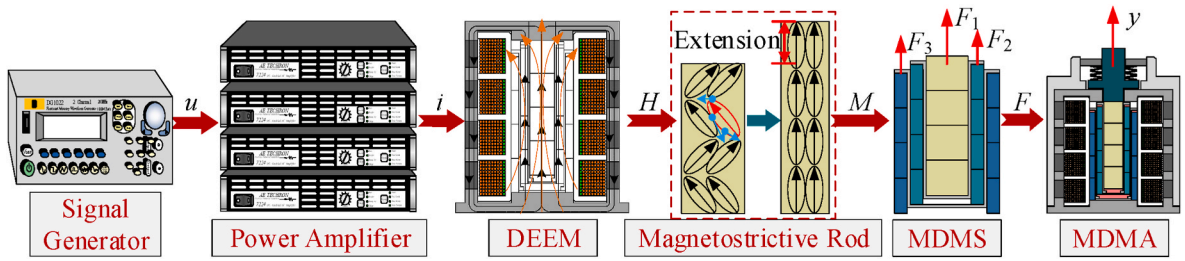

Fig. 2. The working principle of the MDMA. In which, u represents the driving voltage; i represents the driving current; H represents the magnetic field intensity; M represents the magnetization; F represents the magnetostrictive force; y represents the displacement of the MDMA.

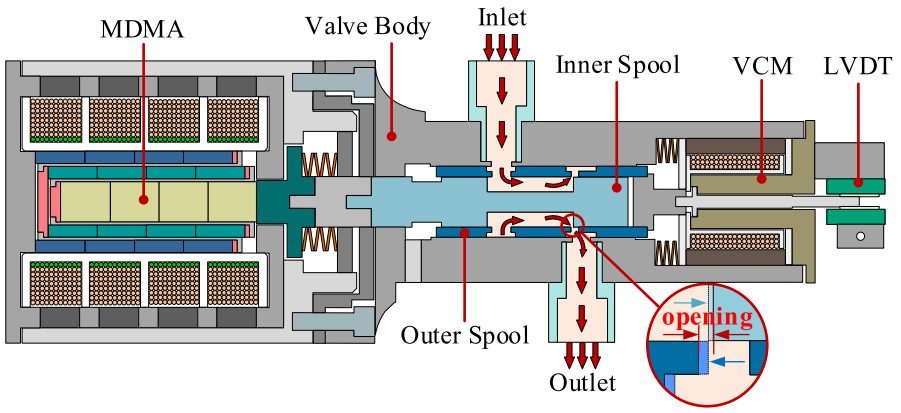

Fig. 3. The architecture of the DSFV. In which, the DSFV mainly consists of the MDMA, the VCM, the inner spool, the outer spool and the valve body.

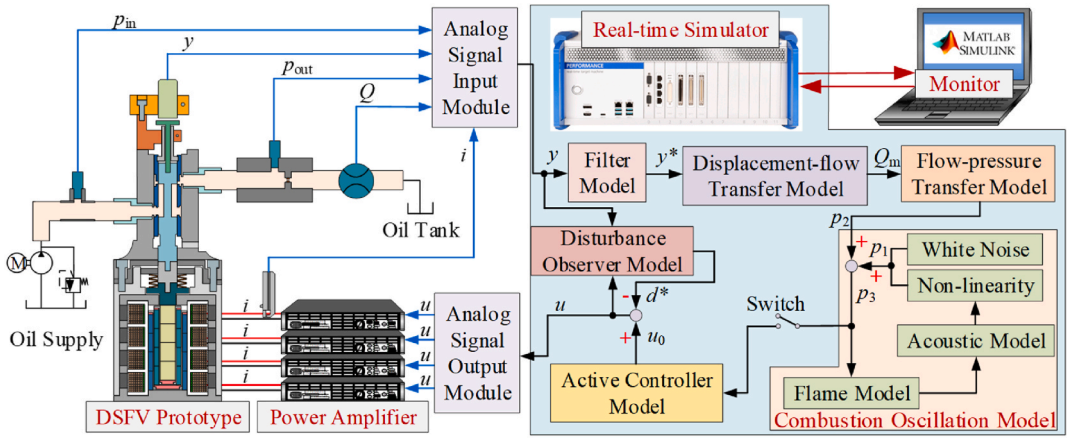

Fig. 4. The diagram of the compositions and working principle of the semi-physical experimental system. In which, all the models are integrated into a real-time simulator, and the physical components mainly include the power amplifiers and the DSFV prototype.

simultaneously as parameters reflecting the operating conditions of the DSFV. Furthermore, No. 10 aviation hydraulic oil was chosen as a substitute for fuel to meet the fuel flow requirements.

In this study, the filter was set as a low-pass filter with a cutoff frequency of 1284.58 Hz, and the flow-pressure transfer model was set a constant gain of 60. Additional models within the system are discussed in the following sections.

3.2. Combustion oscillation model

The combustion oscillation model comprises four fundamental components: the flame model, the acoustic model, the saturation non-linearity model, and the white noise model. The white noise model is employed to induce combustion oscillation, with its power set to 2×10^{-10}, while the flame model, acoustic model, and saturation non-linearity model are specifically designed to simulate the process by which the amplitude of oscillating pressure transitions from zero to a state of saturation. The flame model $G_{\text{flame}}(s)$, acoustic model $G_{\text{acoustic}}(s)$, and saturation non-linearity model $Func(NL)$ are as follows [35]:

$$\begin{cases} G_{\text{flame}}(s) = \dfrac{K_f \omega_f}{s + \omega_f} \\ G_{\text{acoustic}}(s) = \dfrac{K_a \omega_a^2}{s^2 + 2\xi_a \omega_a + \omega_a^2} \\ Func(NL) = \tanh(p) \end{cases} \tag{1}$$

where K_f and ω_f denote the gain and natural frequency of the thermal-acoustic process, respectively. K_a, ω_a and ξ_a represent the gain, natural frequency, and damping ratio of the acoustic-thermal process, respectively. p represents the pressure of the combustion chamber.

To evaluate the efficacy of the active control system utilizing DSFV for suppressing multimodal combustion oscillations, four distinct modes were derived by varying the parameters of the combustion oscillation model, as outlined in Table 1. Among these, Mode 2 was established using empirical high-frequency oscillation measurement data of an actual aeroengine. Fig. 5 illustrates the oscillating pressures process from the zero to saturation in the time domain, as well as the frequency spectrums of the oscillating pressures of the four modes.

Fig. 5 illustrates that all four oscillation modes reach saturation within a duration of 1.5 s, with the amplitudes of normalized pressures recorded post-saturation at 0.48, 0.32, 0.44, and 0.41, respectively. The dominant frequencies of the four oscillation modes are 549.99 Hz, 611.99 Hz, 475.99 Hz, and 593.99 Hz, respectively. The corresponding amplitudes of these dominant frequencies are −9.05 dB, −13.75 dB, −10.25 dB, and −10.63 dB. Consequently, the differences in dominant frequencies and amplitudes reflect the significant variations in

Table 1
The parameters of different combustion oscillation modes.

Mode	K_f	ω_f	K_a	ω_a	ξ_a
Mode 1	1.9	1000	−0.3	3400	0.0707
Mode 2	1.19	3770	−0.25	3612.48	0.0707
Mode 3	1.27	1500	−0.3	2900	0.0707
Mode 4	1.2	2000	−0.3	3600	0.0707

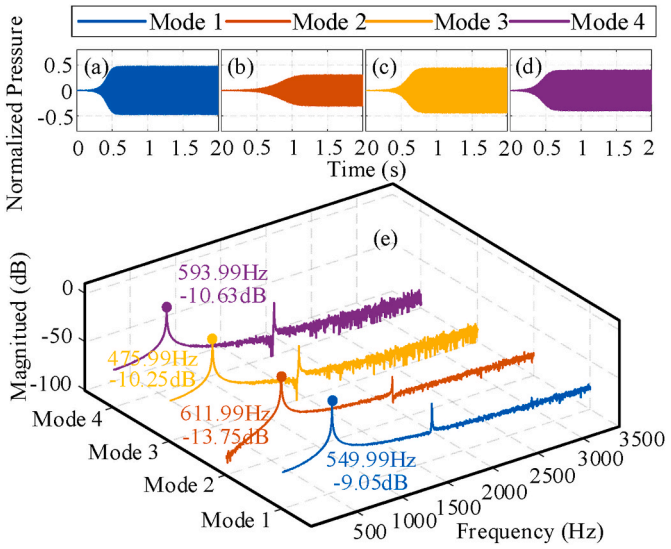

Fig. 5. The variations in the time domain and the frequency spectrums of the four oscillation modes. (a) the variation of Mode 1 in the time domain, (b) the variation of Mode 2 in the time domain, (c) the variation of Mode 3 in the time domain, (d) the variation of Mode 4 in the time domain, (e) the frequency spectrums of the four oscillation modes.

multimodal oscillations.

3.3. Model of the DSFV system

In this paper, we conducted a sinusoidal frequency sweep experiment with an input amplitude of 1 V, where the frequency linearly increased from 10 Hz to 2000 Hz over a duration of 4 s. This experiment aimed to characterize the response behavior of the DSFV system. Using a parameter identification approach, a second-order model $G_n(s)$ was derived to serve as the nominal model of the DSFV system. The transfer function of $G_n(s)$ is as follows:

$$G_n(s) = \frac{9.178 \times 10^8}{s^2 + 3020s + 81662737} \tag{2}$$

The frequency response characteristics of the DSFV system and its corresponding nominal model are illustrated in Fig. 6. The data presented in the figure indicate a close alignment between the amplitude-frequency response curves of the DSFV system and the nominal model. Specifically, the resonant frequency and gain of the DSFV system were recorded at 1376.25 Hz and 32.61 dB, respectively, with an amplitude bandwidth extending to 1951.25 Hz. In comparison, the nominal model exhibited a resonant frequency of 1397.5 Hz and a gain of 30.71 dB.

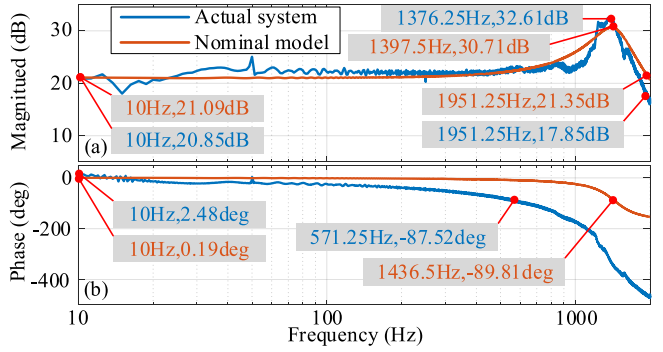

Fig. 6. The frequency response curves of the DSFV system and the nominal model. (a) the amplitude-frequency characteristic curves, (b) the phase-frequency characteristic curves.

Notably, the gain of the DSFV system did not experience a −3 dB day at 1951.28 Hz. Conversely, the phase bandwidth of the nominal model reached 1436.5 Hz, which was considerably greater than the 571.25 Hz bandwidth observed in the DSFV system. Consequently, the discrepancies between the nominal model and the DSFV system may result in discrepancies between the actual output and the anticipated output of the DSFV system, potentially impacting the suppression effects of oscillating pressures. Therefore, it is essential to improve the robustness of the active controller.

3.4. Displacement-flow transfer model

The displacement-flow transfer model illustrates the high-frequency oscillating flow response to the displacement of the inner spool, where the input is the displacement of the inner spool and the output is the high-frequency oscillating flow. Fig. 7 presents a simplified schematic of the fuel flow pipeline within a typical aeroengine.

The fuel, delivered by the fuel supply device, enters the DSFV via the upstream tube. Through high-frequency regulation of the DSFV, the anticipated high-frequency oscillating flow is expected to exit the valve, subsequently flowing through the downstream tube to the nozzle, where it is atomized before entering the combustion chamber for ignition. Ref. [47] conducted theoretical modeling and experimental validation studies on the output high-frequency oscillating flow response to the displacement of the inner spool, which was cited for the semi-physical experimental system discussed in this paper.

Assuming that the flow within the tube is characterized as one-dimensional, inviscid, axisymmetric, and at a low Mach number, and that the tube length is significantly shorter than the acoustic wavelength, the unsteady Bernoulli equation is applicable to the flow in both the upstream and downstream sections of the tube. Furthermore, by taking into account the finite compressibility of the fuel within the cavity V_{in}, the response of the high-frequency flow to the displacement of the inner spool is derived as follows [47]:

$$G_{transfer1}(s) = \frac{Q_m(s)}{X_m(s)} = \frac{-s}{\frac{x_{m0}L_2}{A_{t2}K}s^2 + \frac{1}{\rho A_c}\left(\frac{L_2 A_{t1}}{L_1 A_{t2}} + 1\right)} \tag{3}$$

where $Q_m(s)$ and $X_m(s)$ represent the high-frequency oscillating mass flow and the displacement of the inner spool, respectively. x_{m0} represents the initial axial length of the cavity V_{in}. ρ and K represent the density and isentropic modulus of the fuel, respectively. The values of the relevant parameters for the fuel flow pipeline are presented in Table 2. Therefore, the displacement-flow transfer model in this study is as follows:

$$G_{transfer1}(s) = \frac{-s}{9.49 \times 10^{-8}s + 22.84} \tag{4}$$

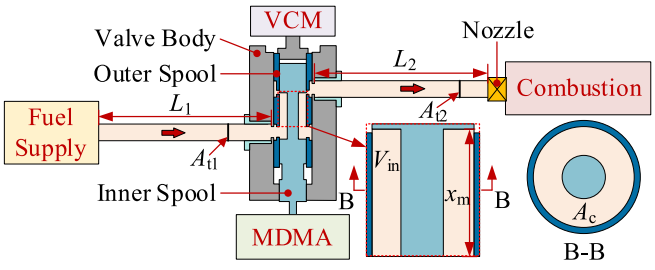

Fig. 7. The simplified schematic of the fuel flow pipeline. In which, x_m represents the axial length of the cavity V_{in}; L_1 and L_2 represent the lengths of the upstream and downstream tubes, respectively; A_{t1}, A_{t2} and A_c represent the cross-sectional areas of the upstream tube, downstream tube, and cavity V_{in}, respectively.

Table 2
The values of the parameters for the fuel flow pipeline.

Parameter	$A_{t1}(m^2)$	$A_{t2}(m^2)$	$A_c(m^2)$	L_1(m)	L_2(m)	K(Pa)	ρ(kg/m^3)	x_{m0}(m)
Value	2.862×10^{-5}	2.862×10^{-5}	6.954×10^{-5}	1	1	1.5×10^{9}	850	0.0122

3.5. Design of active controller

3.5.1. Model of the controlled plant

The design of an H-infinity controller necessitates a linear model of the system being controlled. In this study, the controlled plant consists of several components, including the DSFV system, the filter model, the displacement-flow transfer model, the flow-pressure transfer model, and the combustion oscillation model. Fig. 8 presents the transfer function block diagram, which illustrates the relationship between the input voltage u and the oscillating pressure p_3.

Given that the controller was activated once the oscillating pressure reached saturation, the non-linearity in the combustion oscillation model could be approximated by a fixed gain during the saturation state. The transfer function of the controlled plant is defined as follows:

$$G_{plant}(s) = \frac{P_3(s)}{U(s)} = \frac{G_n(s)\cdot G_{filter}(s)\cdot G_{transfer1}(s)\cdot G_{transfer2}(s)}{1 - G_{flame}(s)\cdot G_{acoustic}(s)\cdot G_{gain}(s)} \tag{5}$$

where $G_n(s)$ is shown as equation (2); $G_{filter}(s)$ is same as equation (11); $G_{transfer1}(s)$ is shown as equation (4); The value of $G_{transfer2}(s)$ is 60; $G_{flame}(s)$ and $G_{acoustic}(s)$ are shown as equation (1). In this paper, oscillation mode 1 was selected as the controller design mode, so that the value of $G_{gain}(s)$ is 0.8487.

3.5.2. Design of H-infinity mixed sensitivity controller

The H-infinity mixed sensitivity controller, which is based on the H-infinity norm, is designed to diminish both external and internal disturbances within specified frequency ranges by adjusting the weighting functions. Fig. 9 illustrates the control block diagram, where the actual controlled plant is integrated with the weighting functions to form the generalized controlled plant.

In Fig. 9, K(s) represents the controller. $G_n(s)$ represents the nominal model of the DSFV system. $G_m(s)$ represents the combined model of the filter, fuel valve, flow-pressure transfer, and combustion oscillation models. d represents the displacement measurement noise. r represents the reference input, which is set to zero in the active control system. e, u, and p represent the tracking error, the controller output, and the oscillating pressure, respectively. $W_1(s)$, $W_2(s)$, and $W_3(s)$ represent the weighting functions for the tracking error, the controller output, and the oscillating pressure, respectively. $Z_1(s)$, $Z_2(s)$, and $Z_3(s)$ represent the evaluation signals for the tracking error, the controller output, and the oscillating pressure, respectively.

The transfer functions from the reference input r to the evaluation signals $Z_1(s)$, $Z_2(s)$, and $Z_3(s)$ are as follows:

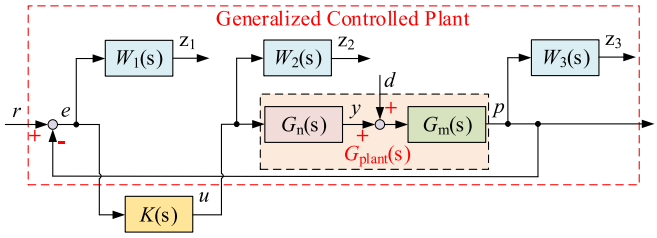

Fig. 9. The control block diagram of the generalized controlled plant.

$$\begin{cases} \dfrac{Z_1}{R} = W_1(s)\dfrac{1}{1 + K(s)G_{plant}(s)} \\ \dfrac{Z_2}{R} = W_2(s)\dfrac{K(s)}{1 + K(s)G_{plant}(s)} \\ \dfrac{Z_3}{R} = W_3(s)\dfrac{K(s)G_{plant}(s)}{1 + K(s)G_{plant}(s)} \end{cases} \tag{6}$$

The sensitivity function, denoted as $S = 1/(1+K(s)G_{plant}(s))$, reflects the system's ability to suppress low-frequency disturbances. A smaller gain of S indicates a greater capacity to diminish these low-frequency disturbances. Conversely, the complementary sensitivity function, denoted as $T = K(s)G_{plant}(s)/(1+K(s)G_{plant}(s))$, reflects the system's ability to suppress the high-frequency disturbances. A smaller gain of T indicates a greater capacity to diminish the high-frequency disturbances. It is important to note that $S + T = 1$, which implies that the suppression of low-frequency and high-frequency disturbances is inherently contradictory. Therefore, a compromise must be achieved by establishing appropriate weighting functions.

To minimize the infinity norm of $W_1(s)/(1+K(s)G_{plant}(s))$, increasing the gain of $W_1(s)$ in the low-frequency range will inevitably lead to a decrease in the gain of S within the same frequency range. Consequently, $W_1(s)$ is typically configured with a high gain in the low-frequency band and a low gain in the high-frequency band. Similarly, $W_3(s)$ is generally configured with a low gain in the low-frequency band and a high gain in the high-frequency band. Additionally, $W_2(s)$ is usually established as a constant to limit the order of the controller. In this study, the transfer functions of the weighting functions are defined as follows:

$$\begin{cases} W_1(s) = \dfrac{0.01s + 20.1}{s + 2.01} \\ W_2(s) = 0.5 \\ W_3(s) = \dfrac{100s + 1000}{s + 100000} \end{cases} \tag{7}$$

Once the weighting functions were determined, the controller $K(s)$ could be computed using the "hinfsyn" function in MATLAB. The initial

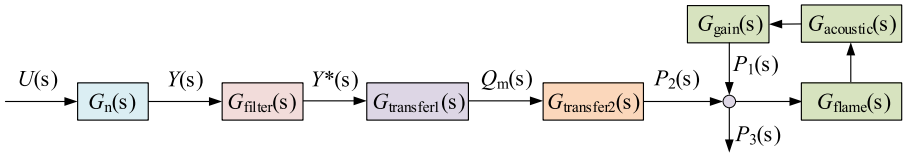

Fig. 8. The transfer function block diagram of the controlled plant. In which, $G_n(s)$ represents the nominal model of the DSFV system; $G_{filter}(s)$ represents the filter model; $G_{transfer1}(s)$ represents the displacement-flow transfer model; $G_{transfer2}(s)$ represents the flow-pressure transfer model; $G_{flame}(s)$ and $G_{acoustic}(s)$ represent the flame model and the acoustic model; $G_{gain}(s)$ represents the fixed saturation gain of the combustion oscillation model.

order of $K(s)$ was 12, which complicated the calculations. To ensure that the frequency characteristics of the controller matched before and after the reduction in the primary working frequency domain, the data fitting method utilizing the "fitrad" function in MATLAB was employed to reduce the order of $K(s)$. The resulting sixth-order model of $K(s)$ is as follows:

$$K(s)=\frac{0.3914s^6+1.28\times10^4s^5-2.24\times10^9s^4-3.95\times10^{12}s^3-1.94\times10^{17}s^2-5.51\times10^{19}s-1.97\times10^{24}}{s^6+1.94\times10^4s^5+5.67\times10^8s^4+6.33\times10^{12}s^3+3.16\times10^{16}s^2+7.35\times10^{19}s+2.76\times10^{23}} \tag{8}$$

3.6. Design of DOB

3.6.1. Structure and working principle of DOB

The structure and working principle of the DOB are illustrated in Fig. 10. The DOB is developed based on the nominal model of the controlled plant, and the discrepancies between the actual and anticipated outputs are treated as equivalent disturbances. Consequently, the DOB introduces appropriate compensation at the input side to effectively diminish these disturbances [48].

In Fig. 10, $G_A(s)$ and $G_n(s)$ represent the actual system and the nominal model of the DSFV system, respectively. u_0, u, and y represent the theoretical input signal, the actual input signal after feedforward compensation, and the output signal of the DSFV system, respectively. d and d^* represent the actual value and the estimated value of the equivalent disturbance, respectively. ζ represents the measurement noise. $Q(s)$ represents the low-pass filter with a steady-state gain of 1, and the relative order of $Q(s)$ is not less than that of the nominal model $G_n(s)$. The transfer function of the output y can be expressed as follows:

$$y=G_{uy}(s)u+G_{dy}(s)d+G_{\zeta y}(s)\zeta \tag{9}$$

Where

$$\begin{cases} G_{uy}(s)=\dfrac{G_A(s)G_n(s)}{G_n(s)+(G_A(s)-G_n(s))Q(s)} \\ G_{dy}(s)=\dfrac{G_A(s)G_n(s)(1-Q(s))}{G_n(s)+(G_A(s)-G_n(s))Q(s)} \\ G_{\zeta y}(s)=\dfrac{G_A(s)Q(s)}{G_n(s)+(G_A(s)-G_n(s))Q(s)} \end{cases} \tag{10}$$

In the low-frequency domain of $Q(s)$, $Q(s)\approx1$, $G_{uy}(s)\approx G_n(s)$, $G_{dy}(s)\approx0$, $G_{\zeta y}(s)\approx1$. While the equivalent disturbance d is diminished, the measurement noise ζ is introduced simultaneously.

In the high-frequency domain of $Q(s)$, $Q(s)\approx0$, $G_{uy}(s)\approx G_A(s)$, $G_{dy}(s)\approx G_A(s)$, $G_{\zeta y}(s)\approx0$. The system behaves similarly to an open-loop system without feedback, which results in the failure to diminish the equivalent disturbance d, although the measurement noise ζ is effectively avoided.

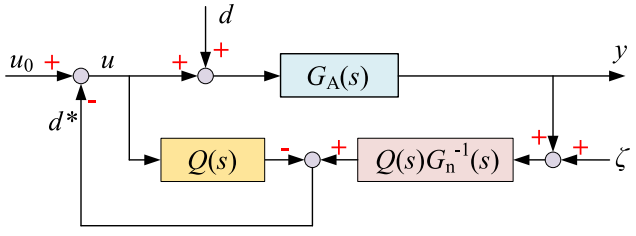

Fig. 10. The structure and working principle of DOB.

3.6.2. Parameters setting of DOB

Consequently, the most critical factor in designing the DOB is the selection of an appropriate model for $Q(s)$ and its corresponding cutoff frequency. In this study, the model for $Q(s)$ was defined as a second-order transfer function, expressed as $Q(s)=1/(\tau^2s^2+2\tau s+1)$. The cutoff frequency of $Q(s)$ can be adjusted by varying the parameter τ. Fig. 11 illustrates the suppression effects on the oscillating pressure of mode 1, as exhibited by six groups of $Q(s)$, each characterized by distinct cutoff frequencies.

Fig. 11(a), (b), and (c) reveal that within the range of cutoff frequencies for $Q(s)$ below 1284.58 Hz, the system exhibited an enhanced ability to suppress oscillating pressure as the cutoff frequency increased. However, the improvement was not significant. In Fig. 11(c), (d), (e), and (f), it became evident that with a further increase in cutoff frequency, the amplitude of the oscillating pressure after active control began to exhibit variability. Notably, when the cutoff frequency reached 2569.16 Hz, there was an increase in the amplitude of the oscillating pressure after active control, indicating a failure in suppressing the oscillating pressure. Therefore, this study established the cutoff frequency of $Q(s)$ at 1284.58 Hz, accompanied by a τ value of 5e-4. The model for $Q(s)$ is as follows:

$$Q(s)=\frac{1}{2.5\times10^{-7}s^2+0.001s+1} \tag{11}$$

Combined with the transfer function of $G_n(s)$, the transfer function of $Q(s)G_n^{-1}(s)$ is as follows:

$$Q(s)G_n^{-1}(s)=\frac{s^2+3020s+81662737}{229.4s^2+917800s+9.18\times10^8} \tag{12}$$

3.7. Prototype of the DSFV

As illustrated in Fig. 12, the magnetostrictive material Terfenol-D was selected for the fabrication of the prototype of the MDMA. Each of the rods, designated as 1, 2, and 3, consists of four short segments, each with an axial length of 10 mm. To ensure optimal performance of the MDMA at elevated temperatures, samarium cobalt, with a Curie temperature of up to 700 °C, was chosen as the material for the permanent magnets. Additionally, polyether-ether-ketone (PEEK), capable of operating at temperatures up to 250 °C, was utilized for the construction of the coil bobbin. The excitation coils were fabricated from copper wire with a diameter of 0.6 mm, comprising a total of 168 × 4 turns multiplied by four. Similarly, the induction coils were constructed from copper wire with a diameter of 0.3 mm, totaling 28 × 4 turns multiplied by four. The magnetic conductors and valve body were made from DT4C, while the sleeves and spools were composed of SUS304. The radial dimensions of the magnetostrictive rods and spools are detailed in Table 3.

3.8. Semi-physical experimental platform

The semi-physical experimental platform designed for the active control of combustion oscillation is illustrated Fig. 13. This platform utilized four power amplifiers (AETechron Inc., 7224) to drive the excitation coils of the MDMA. The current within a excitation coil was monitored using a current transducer (Shenzhen Zhiyong Co., Ltd., Cp800), while the output displacement of the inner spool was measured with a capacitive displacement transducer (Harbin Core Tomorrow

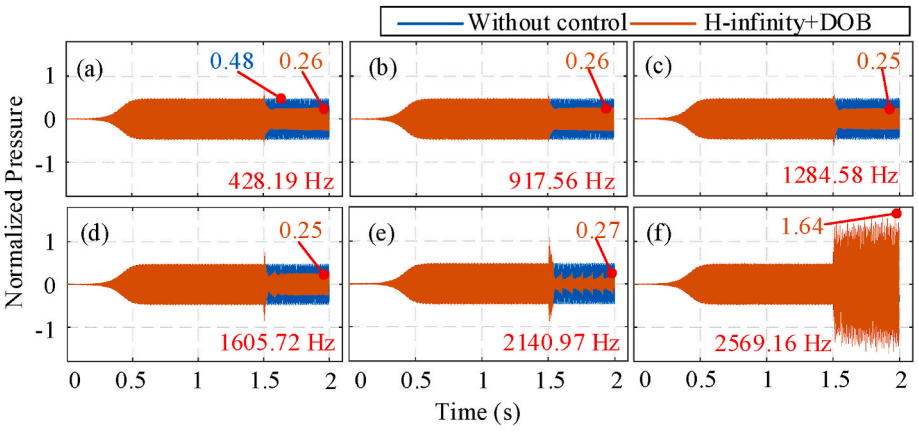

Fig. 11. The suppression effects on oscillation mode 1 at various cutoff frequencies of $Q(s)$. (a) 428.19 Hz, (b) 917.56 Hz, (c) 1284.58 Hz, (d) 1605.72 Hz, (e) 2140.97 Hz, (f) 2569.16 Hz.

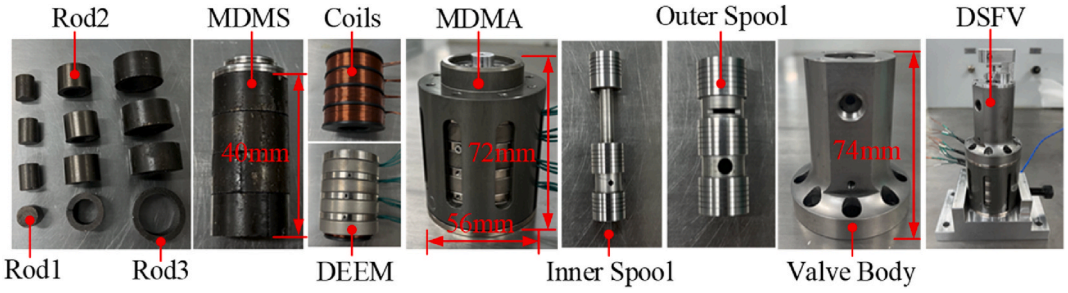

Fig. 12. The prototype of the MDMA and DSFV.

Table 3
The radial dimensions of the three magnetostrictive rods, the inner spool and the outer spool.

Name	Rod 1	Rod 2	Rod 3	Inner spool	Outer spool
Inner diameter (mm)	–	9	15	–	10
Outer diameter (mm)	8	14	20	10	14

Technology Co., Ltd., E09.Cap). The inlet and outlet pressures of the DSFV were recorded using two pressure transducers (Kunshan Shuangqiao Sensor Measurement and Control Technology Co., Ltd., CYG1401F and CYG1531GF, respectively). The oil flow was quantified using a flow transducer (Shanghai Nexon Electronics Co., Ltd., FGR200). A real-time simulator (Speedgoat GmbH, Performance P3) was employed to integrate the models of the semi-physical control system, and an input/output module (Speedgoat GmbH, IO324) was utilized for the transmission and reception of analog signals.

The semi-physical experimental procedure is outlined as follows: Initially, the Simulink real-time simulation model of the semi-physical control system was uploaded to the real-time simulator, with the calculation step set to 0.00001 s. Subsequently, the combustion oscillation model was allowed to reach a saturation state within a duration of 1.5 s, at which point the active controller was activated to generate control signals that facilitate the displacement of the inner spool. After an additional period of 0.5 s, the active controller was deactivated, marking the conclusion of the simulation. In this study, several comparative experiments were conducted by varying the combustion oscillation modes, the controller model, and the inlet oil pressure of the DSFV.

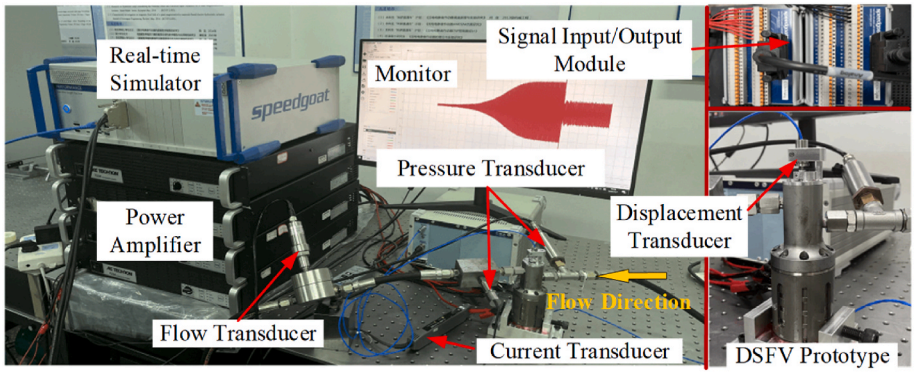

Fig. 13. The diagram of the semi-physical experimental platform.

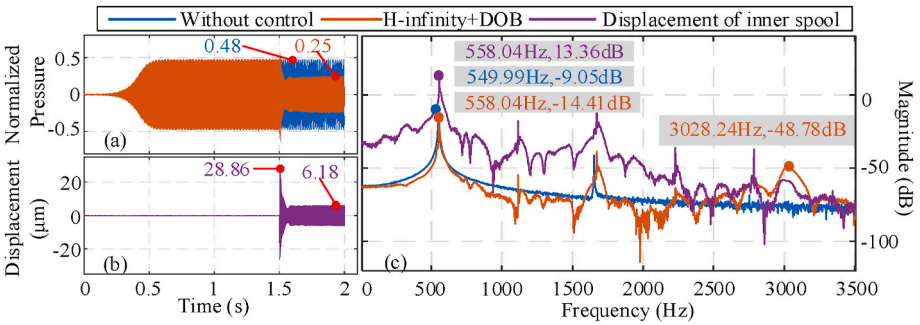

Fig. 14. The suppression result of oscillation mode 1. (a) the oscillating pressure in the time domain, (b) the displacement of the inner spool in the time domain, (c) the frequency spectrums of the oscillating pressure before and after control and that of the displacement of the inner spool from 1.5 to 2 s.

4. Semi-physical experimental result analysis

4.1. Suppression effects of multimodal oscillations

This section investigates the suppression effects of multimodal combustion oscillations under conditions of non-flowing oil. The suppression results for oscillation mode 1 are illustrated in Fig. 14. As shown in Fig. 14(a), following the activation of the active controller, the amplitude of the oscillating pressure experienced a rapid decline from 0.48 to 0.25, subsequently stabilizing. Fig. 14(b) depicts that the amplitude of the inner spool's displacement decreased from 28.86 μm to 6.18 μm before stabilizing, which was consistent with the observed changes in the amplitude of the oscillating pressure. Fig. 14(c) illustrates the frequency spectrums of the oscillating pressure before and after active control, as well as the frequency spectrum of the inner spool's displacement over a time period of 1.5–2 s. Under the influence of the active control system, the amplitude of the dominant frequency of the oscillating pressure decreased from −9.05 dB to −14.41 dB. Notably, after active control, a high-frequency component of the oscillating pressure emerged at a frequency of 3028.24 Hz, with an amplitude of −48.78 dB.

Similarly, the suppression results of oscillation modes 2, 3, and 4 are illustrated in Figs. 15–17, respectively. In the case of oscillation mode 2, the application of active control resulted in a reduction of the oscillating pressure amplitude from 0.32 to 0.15, with the amplitude of the dominant frequency decreasing from −13.75 dB to −24.34 dB. For oscillation mode 3, active control led to a decrease in the oscillating pressure amplitude from 0.44 to 0.09, with the amplitude of the dominant frequency decreasing from −10.25 dB to −21.23 dB. Regarding oscillation mode 4, the oscillating pressure amplitude reduced from 0.41 to 0.15 after active control, and the amplitude of the dominant frequency decreased from −10.63 dB to −17.27 dB. Additionally, similar to oscillation mode 1, the post-control oscillating pressure of these three modes exhibited a high-frequency component of approximately 3000 Hz, with an amplitude of less than −40 dB.

It is typical for the post-control oscillating pressure to induce

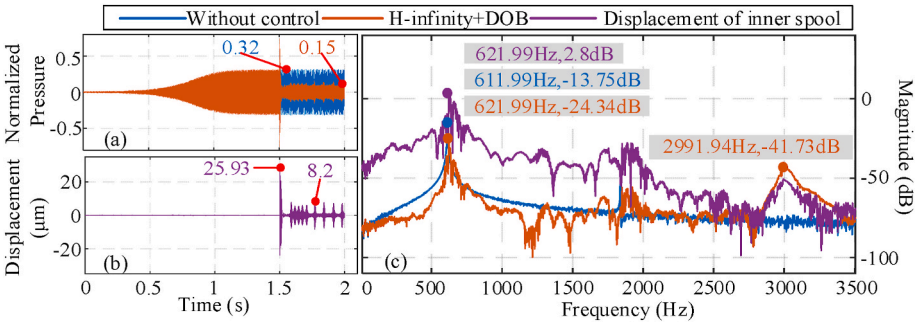

Fig. 15. The suppression result of oscillation mode 2. (a) the oscillating pressure in the time domain, (b) the displacement of the inner spool in the time domain, (c) the frequency spectrums of the oscillating pressure before and after control and that of the displacement of the inner spool from 1.5 to 2 s.

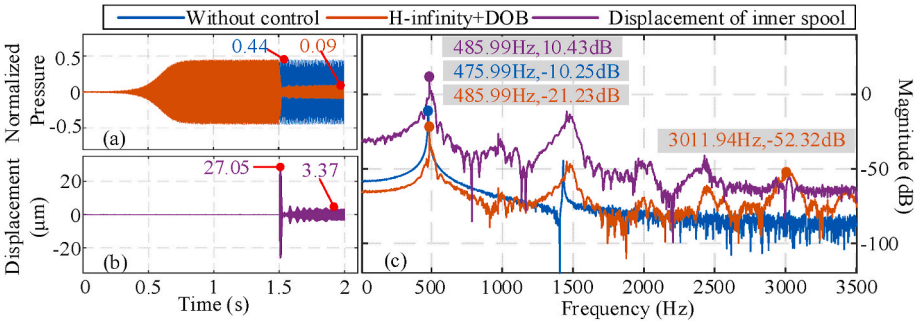

Fig. 16. The suppression result of oscillation mode 3. (a) the oscillating pressure in the time domain, (b) the displacement of the inner spool in the time domain, (c) the frequency spectrums of the oscillating pressure before and after control and that of the displacement of the inner spool from 1.5 to 2 s.

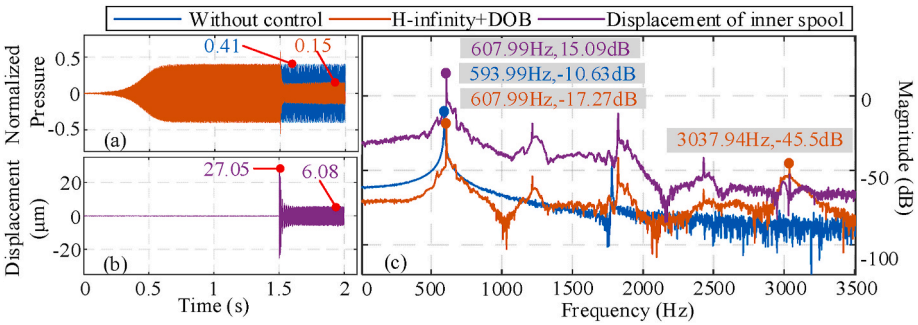

Fig. 17. The suppression result of oscillation mode 4. (a) the oscillating pressure in the time domain, (b) the displacement of the inner spool in the time domain, (c) the frequency spectrums of the oscillating pressure before and after control and that of the displacement of the inner spool from 1.5 to 2 s.

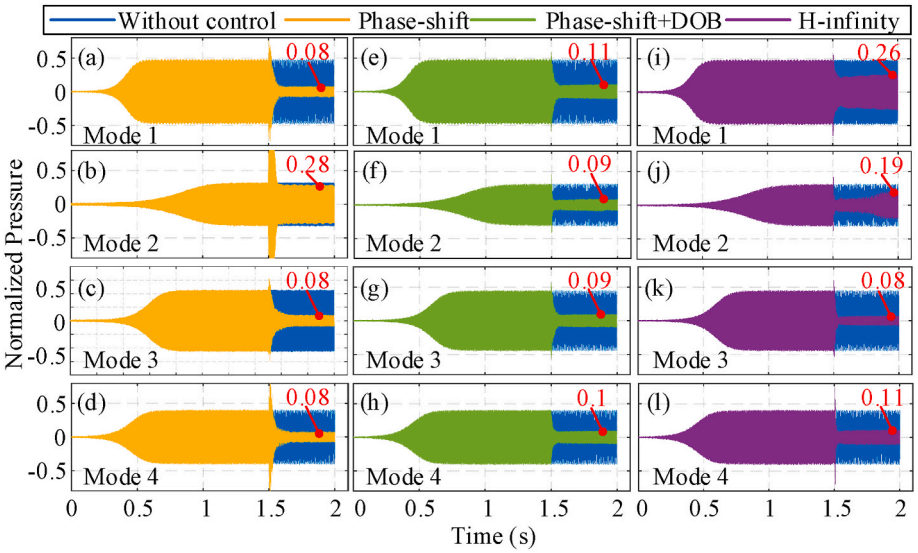

Fig. 18. The suppression effects of multimodal oscillations in different control strategies. In which, (a), (b), (c) and (d) represent the phase-shift control effects; (e), (f), (g) and (h) represent the phase-shift combined DOB control effects; (i), (j), (k) and (l) represent the H-infinity control effects.

additional frequency components, provided that there is a reduction in amplitude in the time domain. The experimental results suggest that the semi-physical experimental system is capable of effectively suppressing multimodal combustion oscillations under conditions of non-flowing oil. Furthermore, the dominant frequencies of the inner spool's displacement corresponded with those of the oscillating pressures, thereby confirming that the DSFV meets the bandwidth requirements of the active control system for high-frequency combustion oscillations.

4.2. Comparison of different control strategies

In this section, several experiments were conducted to verify the superior robustness of the H-infinity combined DOB controller compared to the phase-shift controller, the phase-shift combined DOB controller, and the H-infinity controller. The emergence of a high-frequency component around 3000 Hz in the frequency spectrum of oscillating pressure after active control complicates the evaluation of the four controllers in the frequency domain. Therefore, the subsequent discussion employed the time-domain amplitude of the oscillating pressure as the primary index for comparison. Similar to the design of the H-infinity controller, the parameters of the phase-shift controller were established based on oscillation mode 1, and its transfer function is as follows:

$$G_{ps}(s) = -6 \cdot \exp(0.0001s) \tag{13}$$

Additionally, the models of $Q(s)$ and $Q(s)G_n^{-1}(s)$ in DOB are represented by equations (11) and (12), respectively, while the H-infinity controller model is illustrated in equation (8).

Fig. 18 illustrates the time-domain suppression results for four oscillation modes under conditions of non-flowing oil, utilizing a phase-shift controller, a phase-shift combined DOB controller, and an H-infinity controller. The suppression effects of the H-infinity combined DOB controller have already been illustrated in Figs. 14–16, and Fig. 17. Additionally, Table 4 provides a comparison of the oscillating pressure amplitudes after control. The percentage represents the ratio of the oscillating pressure amplitudes after control relative to those without control.

The results indicate that among the four control strategies, the phase-shift controller demonstrated the least effective control and was unable to adequately suppress oscillation mode 2. In contrast, the phase-shift combined DOB controller achieved the best suppression effects, realizing an average suppression rate of 76.03 %. However, the influence of DOB on the efficacy of the H-infinity controller was minimal. When the

Table 4
The suppression effects of multimodal oscillations in different control strategies.

Oscillation Mode	Phase-shift (%)	Phase-shift + DOB (%)	H-infinity (%)	H-infinity + DOB (%)
Mode 1	83.33	77.08	45.83	47.92
Mode 2	12.5	71.87	40.62	53.12
Mode 3	81.82	79.55	81.82	79.55
Mode 4	80.49	75.61	73.17	63.41
Average	64.54	76.03	60.36	61

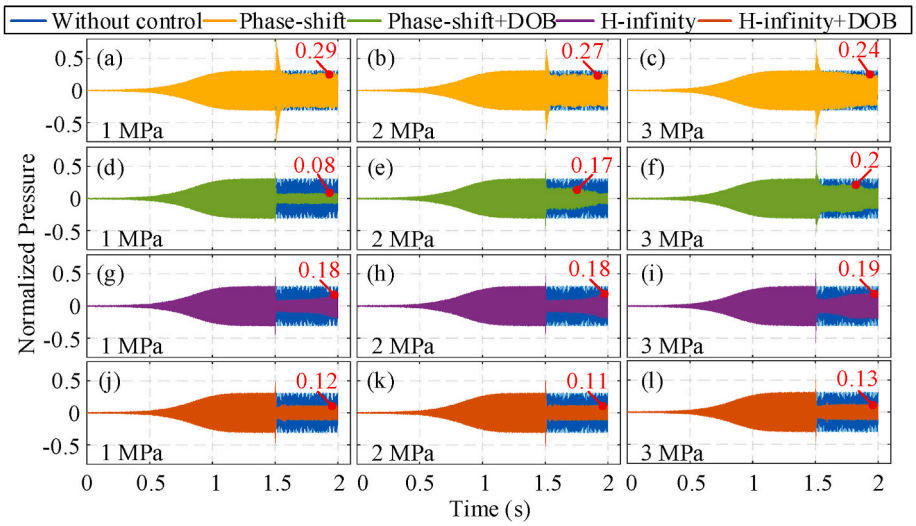

Fig. 19. The suppression effects in different inlet pressures and different control strategies. In which, (a), (b) and (c) represent the phase-shift control effects in different inlet pressures; (d), (e) and (f) represent the phase-shift combined DOB control effects in different inlet pressures; (g), (h) and (i) represent the H-infinity control effects in different inlet pressures; (j), (k) and (l) represent the H-infinity combined DOB control effects in different inlet pressures.

Table 5
The suppression effects in different inlet pressures and different control strategies.

Inlet Pressure	Phase-shift (%)	Phase-shift + DOB (%)	H-infinity (%)	H-infinity + DOB (%)
1 MPa	9.37	75	43.75	62.5
2 MPa	15.62	46.87	43.75	65.62
3 MPa	25	37.5	40.62	59.37
Average	16.67	53.13	42.71	62.5

H-infinity controller was combined with DOB, it resulted in an average suppression effect of 61 %. In comparison, the H-infinity controller applied independently yielded an average suppression effect of 60.36 %.

In the practical application of DSFV, the hydraulic forces generated by the fuel, in conjunction with the frictional forces that differ from those present in non-fuel conditions, further disturb the movement of the inner spool. These disturbances influence the regulation of high-frequency oscillating flow and, consequently, affect the suppression of oscillating pressure. In the following part, several experimental comparisons were conducted to evaluate the suppression effects of the four controllers mentioned above on oscillation mode 2 at inlet pressures of 1 MPa, 2 MPa, and 3 MPa. The results are illustrated in Fig. 19, with detailed data summarized in Table 5.

The experimental results indicate that the phase-shift controller was ineffective in suppressing oscillating pressure. Similarly, although the phase-shift combined DOB controller and the H-infinity controller demonstrated some ability to suppress oscillating pressure, their effectiveness diminished as the inlet pressure increased. A comparative analysis of the suppression effects of the phase-shift combined DOB controller for four oscillation modes without flowing oil, as illustrated in Fig. 18, alongside the results for oscillation mode 2 with flowing oil depicted in Fig. 19, reveals that the DOB could effectively address disturbances arising from variations in oscillation modes. However, it was unable to fully compensate for disturbances caused by the increased hydraulic forces associated with the increasing inlet pressure. In contrast, the H-infinity combined DOB controller exhibited relatively stable suppression effects on oscillating pressures, maintaining an average suppression effect of 62.5 % even as the inlet pressure increased.

5. Conclusion

This paper presents a semi-physical experimental system for the active control of high-frequency combustion oscillation, utilizing a DSFV prototype and a combustion oscillation model. It proposes a control strategy that combines the H-infinity algorithm with a DOB, thereby enhancing the system's robustness and effectively suppressing multimodal combustion oscillations under different operating conditions. The specific conclusions are as follows.

(1) Under conditions of non-oil flowing within the DSFV, thereby excluding the hydraulic forces generated by the oil, a comparative analysis was conducted on the suppression effects of four controllers: a phase-shift controller, a phase-shift combined DOB controller, an H-infinity controller, and an H-infinity combined DOB controller, on multimodal oscillations. The results revealed that the incorporation of the DOB significantly enhanced the anti-disturbance capability of the phase-shift controller. Notably, the phase-shift combined DOB controller achieved an average suppression effect of 76.03 % in the amplitudes of multimodal oscillating pressures, which was superior to the average suppression effect of 61 % of the H-infinity combined DOB controller.

(2) Under conditions of oil flowing within the DSFV, thus accounting for the hydraulic forces generated by the oil, the suppression effects of the aforementioned controllers were evaluated at inlet oil pressures of 1 MPa, 2 MPa, and 3 MPa for a single oscillation mode. The results indicated that the DOB was unable to fully diminish the disturbance induced by hydraulic forces, and the suppression capabilities of the phase-shift combined DOB controller were found to be inadequate. In contrast, the H-infinity combined DOB controller demonstrated effective suppression of oscillating pressures across various inlet pressures, achieving an average suppression effect of 62.5 % in the amplitudes of oscillating pressures.

(3) The semi-physical experimental results indicate that the DSFV shows promise for the active control of high-frequency combustion oscillation in aeroengine. However, it is essential to conduct extensive research on testing methodologies for high-frequency oscillating flow and to establish the high-frequency oscillating

flow model of the DSFV prototype. Such research is crucial for the precise regulation of high-frequency oscillating fuel flow and for meeting the demands of active control of combustion oscillation.

CRediT authorship contribution statement

Chengyuan Li: Writing – original draft, Software, Methodology, Investigation, Formal analysis. **Yuchuan Zhu:** Writing – review & editing, Conceptualization.

Declaration of competing interest

The authors declare that they have no known competing financial interests or personal relationships that could have appeared to influence the work reported in this paper.

Acknowledgements

This work was supported by the National Natural Science Foundation of China (Grant No. 52375059) and the Postgraduate Research & Practice Innovation Program of Jiangsu Province (Grant No. KYCX25_0599).

Data availability

Data will be made available on request.

References

[1] Shi Y, Lu J, Liu X, Lv G, Liu E, Zheng H. Dynamic characteristics analysis under different flame modes in coaxial staged combustor. Aero Sci Technol 2025;162:110181. https://doi.org/10.1016/j.ast.2025.110181.
[2] Lv G, Liu X, Zhang Z, Li S, Liu E, Zheng H. The effects of premixed pilot-stage on combustion instabilities in stratified swirling flames: a large eddy simulation study. Energy 2023;274:127246. https://doi.org/10.1016/j.energy.2023.127246.
[3] Zhao D, Lu Z, Zhao H, Li XY, Wang B, Liu P. A review of active control approaches in stabilizing combustion systems in aerospace industry. Prog Aero Sci 2018;97:35–60. https://doi.org/10.1016/j.paerosci.2018.01.002.
[4] Peng J, Gao L, Yu X, Qin F, Liu B, Cao Z, Han M. Combustion oscillation characteristics of a supersonic ethylene jet flame using high-speed planar laser-induced fluorescence and dynamic mode decomposition. Energy 2022;239:122330. https://doi.org/10.1016/j.energy.2021.122330.
[5] Huang Y, Yang V. Dynamics and stability of lean-premixed swirl-stabilized combustion. Prog Energy Combust Sci 2009;35(4):293–364. https://doi.org/10.1016/j.pecs.2009.01.002.
[6] Tang A, Cai T, Li C, Zhou C, Gao L. Flame visualization and spectral analysis of combustion instability in a premixed methane/air-fueled micro-combustor. Energy 2024;294:130793. https://doi.org/10.1016/j.energy.2024.130793.
[7] Blondé A, Schuermans B, Dharmaputra B, Noiray N. Tunable passive control of thermoacoustic instabilities based on a variable geometry combustor outlet nozzle. Aero Sci Technol 2025;158:109932. https://doi.org/10.1016/j.ast.2025.109932.
[8] Song H, Lin Y, Han X, Yang D, Zhang C, Sung CJ. The thermoacoustic instability in a stratified swirl burner and its passive control by using a slope confinement. Energy 2020;195:116956. https://doi.org/10.1016/j.energy.2020.116956.
[9] Wang K, Hu ZC. Experimental investigation of a novel standing-wave thermoacoustic engine based on PCHE and supercritical CO2. Energy 2023;282:128334. https://doi.org/10.1016/j.energy.2023.128334.
[10] Kang H, Kim KT. Experimental investigation of high-frequency transverse instability in Helmholtz resonator-coupled lean-premixed hydrogen combustor. Int J Hydrogen Energy 2024;65:142–50. https://doi.org/10.1016/j.ijhydene.2024.04.015.
[11] Lei L, Zhihui G, Chengyu Z, Xiaofeng S. A passive method to control combustion instabilities with perforated liner. Chin J Aeronaut 2010;23(6):623–30. https://doi.org/10.1016/S1000-9361(09)60263-6.
[12] Xu L, Zhang G, Wang G, Feng Z, Tian X, Li L, Qi F. Effects of acoustic liner on thermoacoustic instabilities in a premixed swirl combustor. Aero Sci Technol 2021;118:107070. https://doi.org/10.1016/j.ast.2021.107070.
[13] Duan R, Zhang H, Zhang Y, Liu L, Tian L, Zhang X. Effect of longitudinal baffled blades on the first-order tangential acoustic mode in cylindrical chamber. Energy 2019;183:901–11. https://doi.org/10.1016/j.energy.2019.06.101.
[14] Illingworth SJ, Morgans AS. Adaptive feedback control of combustion instability in annular combustors. Combust Sci Technol 2010;182(2):143–64. https://doi.org/10.1080/00102200903258773.
[15] Yilmaz H, Yilmaz I. Flame and instability characteristics of high hydrogen content gas mixtures. Energy 2021;223:120084. https://doi.org/10.1016/j.energy.2021.120084.
[16] Riley AJ, Park S, Dowling AP, Evesque S, Annaswamy AM. Advanced closed-loop control on an atmospheric gaseous lean-premixed combustor. J Eng Gas Turbines Power 2004;126(4):708–16. https://doi.org/10.1115/1.1788685.
[17] Wei W, Wang J, Li DH, Zhu M, Xue YL. Feedback control of combustion oscillations in combustion chambers. Commun Nonlinear Sci Numer Simulat 2010;15(11):3274–83. https://doi.org/10.1016/j.cnsns.2009.12.020.
[18] Richards GA, Thornton JD, Robey EH, Arellano L. Open-loop active control of combustion dynamics on a gas turbine engine. https://doi.org/10.1115/1.2204978; 2007.
[19] Zhong Y, Zhang T, Zhang Y, Cheng T. Flame temperature and heat release rate sensor for active combustion control. Measurement 2022;202:111762. https://doi.org/10.1016/j.measurement.2022.111762.
[20] Li F, Luo H, Du J, Yuan M, Lin F, Nie C. Plasma pressure sensor based on direct current glow discharge. Aero Sci Technol 2020;106:106069. https://doi.org/10.1016/j.ast.2020.106069.
[21] Gelbert G, Moeck JP, Paschereit CO, King R. Feedback control of unstable thermoacoustic modes in an annular Rijke tube. Control Eng Pract 2012;20(8):770–82. https://doi.org/10.1016/j.conengprac.2012.03.016.
[22] Yazar I, Caliskan F, Vepa R. Model predictive control and controller parameter optimisation of combustion instabilities. Int J Turbo Jet Engines 2019;36(2):185–94. https://doi.org/10.1515/tjj-2017-0062.
[23] Zhang L, Su X, Zhou H, Wang X, Ren Z. Active control of multiple neural networks for oscillating combustion. AIAA J 2022;60(6):3821–33. https://doi.org/10.2514/1.J061370.
[24] Yuan XC, Glover K. Model-based control of thermoacoustic instabilities in partially premixed lean combustion–a design case study. Int J Control 2013;86(11):2052–66. https://doi.org/10.1080/00207179.2013.830337.
[25] Cheng T, Zhang T, Zhong Y, Ji H, Zhang X. Design and experimental validation of active robust controller for the jet flame combustion oscillation. Int J Therm Sci 2024;197:108787. https://doi.org/10.1016/j.ijthermalsci.2023.108787.
[26] Nabae H, Higuchi T. A novel electromagnetic actuator based on displacement amplification mechanism. IEEE ASME Trans Mechatron 2014;20(4):1607–15. https://doi.org/10.1109/TMECH.2014.2360316.
[27] Guo H, Wang D, Xu J. Research on a high-frequency response direct drive valve system based on voice coil motor. IEEE Trans Power Electron 2012;28(5):2483–92. https://doi.org/10.1109/TPEL.2012.2213345.
[28] DeLaat J, Breisacher K, Saus J, Paxson D. Active combustion control for aircraft gas turbine engines. In: 36th AIAA/ASME/SAE/ASEE joint propulsion conference and exhibit; 2000, July. p. 3500. https://doi.org/10.2514/6.2000-3500.
[29] Burkhardt WM, Crapuchettes JM. U.S. patent no. 10,697,373. Washington, DC: U.S. Patent and Trademark Office; 2020.
[30] Chen L, Zhu Y, Ling J. Development and characteristic analysis of a double spool nested fuel valve. In: 2023 9th international conference on fluid power and mechatronics (FPM). IEEE; 2023, August. p. 1–5. https://doi.org/10.1109/FPM57590.2023.10565525.
[31] Chen L, Zhu Y, Ling J, Zhang M. Development and characteristic investigation of a multidimensional discrete magnetostrictive actuator. IEEE ASME Trans Mechatron 2022;27(4):2071–9. https://doi.org/10.1109/TMECH.2022.3173619.
[32] Chen L, Zhu Y, Ling J, Zhang M. Temperature dependence modeling and experimental evaluation of a multidimensional discrete magnetostrictive actuator. Appl Therm Eng 2023;230:120736. https://doi.org/10.1016/j.applthermaleng.2023.120736.
[33] Neumeier Y, Zinn B. Active control of combustion instabilities with real time operation of unstable combustor modes. In: 34th aerospace sciences meeting and exhibit; 1996, January. p. 758. https://doi.org/10.2514/6.1996-758.
[34] Johnson CE, Neumeier Y, Neumaier M, Zinn BT, Darling DD, Sattinger SS. Demonstration of active control of combustion instabilities on a full-scale gas turbine combustor. In: Turbo expo: power for land, Sea, and air, vol.78514. American Society of Mechanical Engineers; 2001, June, V002T02A062. https://doi.org/10.1115/2001-GT-0519.
[35] Kopasakis G. High frequency adaptive instability suppression controls in a liquid-fueled combustor. In: 39th AIAA/ASME/SAE/ASEE joint propulsion conference and exhibit; 2003, July. p. 4491. https://doi.org/10.2514/6.2003-4491.
[36] Zhou H, Tao C, Liu Z, Meng S, Cen K. Optimal control of turbulent premixed combustion instability with annular micropore air jets. Aero Sci Technol 2020;98:105650. https://doi.org/10.1016/j.ast.2019.105650.
[37] Liu Y, Li J, Zhang T, Yan Y. Active suppression of swirl-stabilized combustion instability. Fuel 2021;287:119559. https://doi.org/10.1016/j.fuel.2020.119559.
[38] Wu G, Xu X, Li S, Ji C. Experimental studies of mitigating premixed flame-excited thermoacoustic oscillations in T-shaped combustor using an electrical heater. Energy 2019;174:1276–82. https://doi.org/10.1016/j.energy.2019.03.042.
[39] Rubio-Hervas J, Zhao D, Reyhanoglu M. Nonlinear feedback control of self-sustained thermoacoustic oscillations. Aero Sci Technol 2015;41:209–15. https://doi.org/10.1016/j.ast.2014.12.026.
[40] Li J, Morgans AS. Simplified models for the thermodynamic properties along a combustor and their effect on thermoacoustic instability prediction. Fuel 2016;184:735–48. https://doi.org/10.1016/j.fuel.2016.07.050.
[41] Kopasakis G, DeLaat JC, Chang CT. Adaptive instability suppression controls method for aircraft gas turbine engine combustors. J Propul Power 2009;25(3):618–27. https://doi.org/10.2514/1.36777.
[42] Yi T, Gutmark EJ. Combustion instabilities and control of a multiswirl atmospheric combustor. J Eng Gas Turbines Power 2007;129(1):31–7. https://doi.org/10.1115/1.2181595.
[43] Seume J, Votmeyer N, Krause W, Hermann J, Hantschk C, Zangl P, Gleis S, Vortmeyer D, Orthmann A. Application of active combustion instability control to a

heavy duty gas turbine. J Eng Gas Turbines Power 1998;120(4):721–6. https://doi.org/10.1115/1.2818459.
[44] Fung YT, Yang V. Active control of nonlinear pressure oscillations in combustion chambers. J Propul Power 1992;8(6):1282–9. https://doi.org/10.2514/3.11474.
[45] Zhang L, Liu QZ, Fan GW, Lv XY, Gao Y, Xiao Y. Parametric control for flexible spacecraft attitude maneuver based on disturbance observer. Aero Sci Technol 2022;130:107952. https://doi.org/10.1016/j.ast.2022.107952.
[46] Yi J, Chang S, Shen Y. Disturbance-observer-based hysteresis compensation for piezoelectric actuators. IEEE/ASME Trans Mech 2009;14(4):456–64. https://doi.org/10.1109/TMECH.2009.2023986.
[47] Yi T, Gutmark EJ. Dynamics of a high-frequency fuel actuator and its applications for combustion instability control. J Eng Gas Turbines Power 2007;129(3):648–54. https://doi.org/10.1115/1.2718558.
[48] Chen XS, Yang J, Li SH, Li Q. Disturbance observer based multi-variable control of ball mill grinding circuits. J Process Control 2009;19(7):1205–13. https://doi.org/10.1016/j.jprocont.2009.02.004.